

# cuIBM – A GPU-accelerated Immersed Boundary Method

S. K. Layton<sup>a</sup>, Anush Krishnan<sup>a</sup>, L. A. Barba<sup>a,\*</sup>

<sup>a</sup>Department of Mechanical Engineering, Boston University, Boston, MA, 02215, USA.

## Abstract

A projection-based immersed boundary method is dominated by sparse linear algebra routines. Using the open-source *Cusp* library, we observe a speedup (with respect to a single CPU core) which reflects the constraints of a bandwidth-dominated problem on the GPU. Nevertheless, GPUs offer the capacity to solve large problems on commodity hardware. This work includes validation and a convergence study of the GPU-accelerated IBM, and various optimizations.

**Keywords:** Immersed Boundary Method, Computational Fluid Dynamics, GPU Computing

## 1. Introduction

The immersed boundary method (IBM) refers to a general class of techniques in computational fluid dynamics, characterized by the solution of the incompressible Navier-Stokes equations on a grid that does not conform to the immersed solid body present in the fluid. Conventional CFD techniques require the generation of a mesh that conforms to the geometry of the domain on which the equations are solved. In the immersed boundary method, the fluid is represented by an Eulerian grid (typically a Cartesian grid) and the solid boundary is represented by a collection of Lagrangian points. This has several advantages. Mesh generation is trivial, and simulations involving moving solid bodies and boundaries are made simpler. The Navier-Stokes equations are solved on the entire grid (including points within the solid), and the effect of the solid body is modelled by adding a singular force distribution  $\mathbf{f}$  along the solid boundary which enforces the no-slip condition. The governing equations are,

$$\frac{\partial \mathbf{u}}{\partial t} + \mathbf{u} \cdot \nabla \mathbf{u} = -\nabla p + \nu \Delta \mathbf{u} + \int_s \mathbf{f}(\xi(s, t)) \delta(\xi - \mathbf{x}) ds \quad (1a)$$

$$\nabla \cdot \mathbf{u} = 0 \quad (1b)$$

$$\begin{aligned} \mathbf{u}(\xi(s, t)) &= \int_s \mathbf{u}(\mathbf{x}) \delta(\mathbf{x} - \xi) d\mathbf{x} \\ &= \mathbf{u}_B(\xi(s, t)), \end{aligned} \quad (1c)$$

where  $\mathbf{u}_B$  is the velocity of the body at the boundary point locations. The different IBM formulations use different techniques to calculate this forcing term.

The immersed boundary method was introduced in 1972 by C S Peskin [21] to model blood flow through the elastic membranes of the heart. The technique has since been extended

to simulate rigid bodies, and the IBM has seen renewed interest in recent times. Mittal and Iaccarino [17] provide a good overview, discussing various techniques that have been used to impose the no-slip condition on immersed boundaries.

Peskin [21] proposed modelling the body as a collection of springs, with boundary points placed at the equilibrium positions of the springs and allowed to move with the flow, and the force calculated using Hooke's law. The force is transferred from the solid to the fluid grid by using a well-chosen discretized approximation to the Dirac delta function. A second-order accurate extension to this method was developed in [12].

Goldstein *et al.* [6] generalised this technique by using a singular force at the boundary points, given by  $\mathbf{F}(\mathbf{x}_s, t) = \alpha \int_0^t (\mathbf{u}(\mathbf{x}_s, t) - \mathbf{v}(\mathbf{x}_s, t)) dt + \beta (\mathbf{u}(\mathbf{x}_s, t) - \mathbf{v}(\mathbf{x}_s, t))$ , where  $\alpha$  and  $\beta$  are constants that are chosen depending on the physical characteristics of the flow. This forcing function enforces the no-slip condition at the solid surface by means of a feedback loop. Saiki and Biringen [23] used this technique in conjunction with the finite difference method. Note that we obtain the same method as [12] by setting  $\beta$  to zero.

These methods are easy to implement but have some shortcomings. The no-slip condition is not directly applied, and it takes some time for the system to attain it. The algorithms also depend on *ad hoc* parameters that need to be chosen carefully depending on the physics of the flow and the desired accuracy. The typically large values of the parameters also place a very strict restriction on the time step due to stability constraints.

Mohd-Yusof [19] formulated a method in which the forcing term is directly obtained from the discretised Navier-Stokes equations by assuming no-slip at the solid boundaries. The velocity at the grid points near the boundary is estimated via interpolation and the forcing term is calculated by

$$\mathbf{f} = \rho \left( \frac{\partial \mathbf{u}}{\partial t} + \mathbf{u} \cdot \nabla \mathbf{u} \right) + \nabla p - \mu \Delta \mathbf{u}. \quad (2)$$

This technique was implemented by Fadlun *et al.* [4]. An implicit scheme to calculate the diffusion and the forcing term allowed large CFL numbers of the order of  $10^{-1}$  to be used. This

\*Correspondence: 110 Cummington St, Boston MA 02215, (617) 353-3883  
Email addresses: slayton@bu.edu (S. K. Layton), anush@bu.edu (Anush Krishnan), labarba@bu.edu (L. A. Barba)

method does not exactly satisfy the no-slip condition, but the errors were shown to be small. Kim *et al.* [10] used a similar idea, with the addition of a mass source at the boundaries. The forcing term and mass sources were calculated explicitly, which placed a stricter restriction on the time step.

Uhlmann [29] reported that the method in [4] produced a boundary force that was not smooth in time when it was used to solve flows with moving boundaries. To fix this, he recommended calculating the singular force distribution at the Lagrangian body points and then distributing the force on the Eulerian grid by using a discrete delta function, rather than calculating the forcing term directly. This method too does not satisfy the no-slip condition exactly and has the stricter time step restriction, but eliminated the force oscillations.

The *immersed boundary projection method* was introduced by Taira and Colonius [24], based on an extension of the projection method [2, 9, 20] used to solve the incompressible Navier-Stokes equations. Using the idea that the pressure in incompressible flows acts as a Lagrangian multiplier to ensure the zero-divergence condition, they similarly consider the forcing term as Lagrangian multiplier that ensures the no-slip condition on the immersed boundary. During the projection step, the velocity field is adjusted such that both these constraints are satisfied exactly. An implicit scheme used for diffusion allows the usage of relatively large time steps, with CFL numbers as high as 1. They later used a nullspace approach that sped up the simulation by up to two orders of magnitude [3]. This approach essentially uses a spectral method to solve the equations cast in the velocity-vorticity formulation.

The techniques described so far make use of some kind of interpolation to transfer the singular forces at the boundary to the Eulerian grid on which the Navier-Stokes equations are solved. This causes the boundary to appear diffused and affects the accuracy of the boundary layer. Boundary layers need to be resolved more accurately at higher Reynolds numbers, and so a number of *sharp-interface* methods have been developed to handle this problem. Among them is the cut-cell method. Cells near the boundary are cut to shapes that conform to the body, and the rest of the grid is Cartesian. The Navier-Stokes equations are solved using the finite volume method in all the cells that contain the fluid and no forcing term is used. Both local and global conservation of properties in the domain can be ensured. This technique has been used by Ye *et al.* [32], Udaykumar *et al.* [26, 27, 28], Mittal *et al.* [16, 18] and Marella *et al.* [15]. Extending this procedure to three dimensions is non-trivial due to the complex shapes that can be formed by cutting.

Another sharp-interface method is known as the ghost-cell method. Here, an interpolation scheme is used at the interface to calculate flow properties at the grid points, implicitly taking into account the boundary conditions. This technique has been used by Majumdar *et al.* [14], Iaccarino and Verzicco [7], Ghias *et al.* [5] and Kalitzin *et al.* [8], the last two of whom carried out turbulence simulations.

In the present work, we use the algorithm presented in [24] for the solution of two-dimensional incompressible viscous flows with immersed boundaries, which is explained in detail in §2. We have produced an implementation on GPU hard-

ware, studying techniques that provide good performance in this multi-threaded architecture, which are described in some detail. The various challenges that an efficient implementation on GPU pose are representative of those that practitioners of other CFD methods would face. Thus, we hope to contribute to the ongoing investigations on the use of GPU hardware for computational fluid dynamics. To our knowledge, the IBM has not previously been implemented on the GPU. The perspective of doing so is the capacity of solving large three-dimensional moving boundary problems on commodity hardware.

## 2. Immersed Boundary Projection Method

We implement the method proposed by Taira & Colonius [24]. The Navier-Stokes equations (1a)–(1c) are discretised on a staggered cartesian grid. The grid can be non-uniform, and it is advantageous to stretch the grid away from the high vorticity regions to reduce the number of grid points without sacrificing accuracy. We obtain the following set of algebraic equations:

$$\begin{aligned}\hat{A}u^{n+1} - \hat{r}^n &= -\hat{G}\phi + \hat{b}c_1 + \hat{H}f \\ \hat{D}u^{n+1} &= bc_2 \\ \hat{E}u^{n+1} &= u_B^{n+1},\end{aligned}\quad (3)$$

which can be written as:

$$\begin{pmatrix} \hat{A} & \hat{G} & \hat{H} \\ \hat{D} & 0 & 0 \\ \hat{E} & 0 & 0 \end{pmatrix} \begin{pmatrix} u^{n+1} \\ \phi \\ f \end{pmatrix} = \begin{pmatrix} \hat{r}^n \\ 0 \\ u_B^{n+1} \end{pmatrix} + \begin{pmatrix} \hat{b}c_1 \\ -bc_2 \\ 0 \end{pmatrix}\quad (4)$$

where  $\phi$  and  $f$  are vectors whose contents are the pressure and the components of the forces at the immersed boundary points respectively. The velocity at the current time step  $u^n$  is known.  $\hat{b}c_1$  and  $bc_2$  are obtained from the boundary conditions on the velocity.

$\hat{H}$  and  $\hat{E}$  are the regularisation and interpolation matrices respectively, which are used to transfer values of the flow variables between the Eulerian and Lagrangian grids. The interpolation in (1c) can be discretised as:

$$u_k = \sum_i u_i d(x_i - \xi_k) d(y_i - \eta_k) \Delta x \Delta y, \quad (5)$$

where  $u_k$  is the velocity at a point  $(\xi_k, \eta_k)$  on the immersed boundary.  $u_k$  is calculated by convolving the velocities on the Eulerian grid  $u_i$  at locations  $(x_i, y_i)$  with a discrete two-dimensional delta function. The discrete delta function is a product of smoothed one-dimensional delta functions  $d_h(r)$  along each Cartesian direction. We choose the one used by Roma *et al* [22]:

$$d_h(r) = \begin{cases} \frac{1}{6h} \left( 5 - 3\frac{|r|}{h} - \sqrt{-3\left(1 - \frac{|r|}{h}\right)^2 + 1} \right), & 0.5 < \frac{|r|}{h} \leq 1.5 \\ \frac{1}{3h} \left( 1 + \sqrt{-3\left(\frac{|r|}{h}\right)^2 + 1} \right), & 0 < \frac{|r|}{h} \leq 0.5 \\ 0, & \text{otherwise,} \end{cases}$$

where  $h$  is the cell width. Use of the discrete delta function requires the grid to be uniform near the immersed boundary. Sufficient number of boundary points need to be chosen to prevent flow leakage, and the spacing between boundary points should be around the same as the cell width of the Eulerian grid.

From the above, we can calculate the elements of matrix  $\hat{E}$ :

$$\hat{E}_{k,i} = \Delta x \Delta y d(x_i - \xi_k) d(y_i - \eta_k). \quad (6)$$

The matrix  $\hat{H}$  is similarly determined by discretising the forcing term in (1a).

The explicit second-order Adams-Bashforth scheme is used to discretise the convection terms and the Crank-Nicolson scheme is used for diffusion. All spatial derivatives are calculated using central differences. Note that no explicit pressure boundary conditions need to be specified. The pressure and body forces are calculated implicitly. The above system of equations can be solved to obtain the velocity field at time step  $n + 1$ , the pressure (to a constant) and the body forces. But the left-hand side matrix is indefinite, and solving the system directly is ill-advised.

By performing appropriate transformations (see Appendix of [24] for details), we can show that the above system is equivalent to:

$$\begin{pmatrix} A & G & E^T \\ G^T & 0 & 0 \\ E & 0 & 0 \end{pmatrix} \begin{pmatrix} q^{n+1} \\ \phi \\ \tilde{f} \end{pmatrix} = \begin{pmatrix} r^n \\ 0 \\ u_B^{n+1} \end{pmatrix} + \begin{pmatrix} bc_1 \\ -bc_2 \\ 0 \end{pmatrix} \quad (7)$$

where  $q^{n+1}$  is the momentum flux at each cell boundary, and the sub-matrices are transformed versions of those in (4). We can rewrite the above by combining some of the sub-matrices in the following manner:

$$Q = \begin{bmatrix} G & E^T \end{bmatrix}, \quad \lambda = \begin{pmatrix} \phi \\ \tilde{f} \end{pmatrix}, \quad r_1 = r^n + bc_1, \quad r_2 = \begin{pmatrix} -bc_2 \\ u_B^{n+1} \end{pmatrix} \quad (8)$$

which gives us

$$\begin{pmatrix} A & Q \\ Q^T & 0 \end{pmatrix} \begin{pmatrix} q^{n+1} \\ \lambda \end{pmatrix} = \begin{pmatrix} r_1 \\ r_2 \end{pmatrix} \quad (9)$$

Applying the approximate factorisation described in [20] to the above system, we obtain the following set of equations which can be solved to give us the velocity distribution at time step  $n + 1$ :

$$Aq^* = r_1 \quad (10a)$$

$$Q^T B^N Q \lambda = Q^T q^* - r_2 \quad (10b)$$

$$q^{n+1} = q^* - B^N Q \lambda \quad (10c)$$

where  $B^N$  is an  $N^{\text{th}}$  order approximation of  $A^{-1}$ . This must be taken into account while estimating the overall time accuracy of the method.

This factorisation is very advantageous as the two linear systems (10a) and (10b) that we now need to solve can be made

positive definite, and can be solved efficiently using the conjugate gradient method. In the absence of an immersed boundary, this set of equations is the same as that solved in the traditional fractional step method or projection method [20, 9, 2]. The final equation (10c) simultaneously ensures a divergence-free velocity field and the no-slip condition in the next time step. By virtue of the above formulation, no special boundary conditions need to be derived for  $q^*$  or  $\lambda$ . As is usual, one value of pressure needs to be pinned to obtain a unique solution since the left hand side matrix  $Q^T B^N Q$  in (10c) has one eigenvalue which is zero.

### 3. Assessment of iterative solvers for the IBM

Like a majority of numerical methods used in computational mechanics, the IBM requires tools for sparse linear algebra. The matrices  $A$ ,  $Q$  and  $Q^T$  are sparse, the vectors  $q^{n+1}$  and  $\lambda$  are dense, and we need to operate on these objects via matrix-vector, matrix-matrix, and even a triple-matrix multiplication. To take advantage of the GPU, we need efficient means of both representing and operating on these matrices and vectors on the device. Currently, there are two tools available for this purpose: CUSPARSE, part of NVIDIA's CUDA, or the external library, *Cusp*. The *Cusp* library is being developed by several NVIDIA employees with minimal software dependencies and released freely under an open-source license. We chose to use the *Cusp* library for several reasons: it is actively developed and separate from the main CUDA distribution, allowing for faster addition of new features (such as new pre-conditioners, solvers, *etc.*); and, all objects/methods from the library are usable on both CPU and GPU. This allows us the flexibility to, for example, perform branching-heavy code on the CPU, before trivially transferring to the device and running (for instance) a linear solve, where it will be significantly faster. It also allows us to maintain both a CPU and GPU code with less effort.

To illustrate the importance of having efficient linear algebra methods, we show in Figure 1a a breakdown of the timings from an example run on the GPU the with the IBM (4000 time steps of a flapping airfoil at  $Re = 75$ ). The mesh consists of  $930 \times 654$  cells, resulting in systems of over 600,000 unknowns. Even in this moderately sized test, the runtime is dominated by the solution of the coupled linear system for pressure and forcing terms, denoted by 'Solve 2'. Speeding up this linear solve is the major motivation for using the GPU.

At this point, it is interesting to consider the potential benefits of using the GPU for our linear systems. Sparse linear systems are a well known example of a bandwidth-limited problem—the potential speedup from using a GPU will at best be the ratio of the bandwidths of the CPU and GPU used. For the Intel Xeon X5650 processors in our workstation, Intel quotes a maximum bandwidth of 32 GB/s<sup>1</sup>, while NVIDIA quotes 144 GB/s for the Tesla C2050 cards we use<sup>2</sup>. Using these numbers, we can see that the best-case speedup should be 4.5× for

<sup>1</sup>[http://ark.intel.com/products/47922/Intel-Xeon-Processor-X5650-\(12M-Cache-2.66-GHz-6.40-GTs-Intel-QPI\)](http://ark.intel.com/products/47922/Intel-Xeon-Processor-X5650-(12M-Cache-2.66-GHz-6.40-GTs-Intel-QPI))

<sup>2</sup>[http://www.nvidia.com/docs/IO/43395/NV\\_DS\\_Tesla\\_C2050\\_C2070\\_jul10\\_lores.pdf](http://www.nvidia.com/docs/IO/43395/NV_DS_Tesla_C2050_C2070_jul10_lores.pdf)

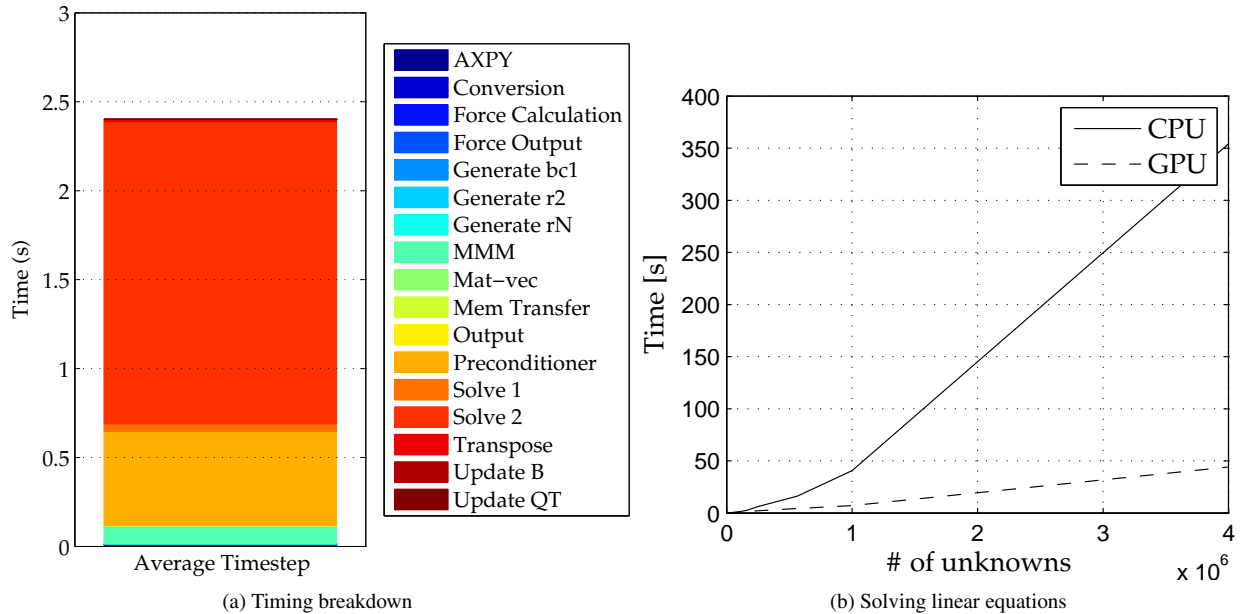


Figure 1: (a) Timing breakdown for a flapping airfoil at  $Re = 75$  using the GPU code. (b) Comparison of time taken to solve a system of linear equations  $Ax = b$  on the CPU and GPU.  $A$  is chosen as the standard 5-pt Poisson stencil.

a purely bandwidth-bound problem, while for computationally bound problems the speedup can be much higher. In practice, even the worst case speedup is definitely worthwhile, certainly enough to justify the extra complexity involved in using the GPU.

Figure 1b shows a timing comparison between the CPU and GPU using *Cusp*'s conjugate gradient solver. The system being solved in this case is given by a traditional 5-point Poisson stencil, which while not directly used in the IBM code, gives a good measure of relative performance that can potentially be obtained. The plot shows the wall-clock time required to solve to a relative accuracy of  $10^{-5}$  for numbers of unknowns ranging from 2500 to  $4 \times 10^6$ . For large systems, the GPU solve is significantly faster, with a speedup of  $8\times$  for the largest system shown. This indicates that even though our actual system may be much harder to solve, the potential speedup is significant.

For the particular linear system we're interested in, we also have to take into account that it has an unusual non-zero structure, shown in Figure 2, due to the coupled nature of the variables being solved for (pressure and forcing terms). This coupled nature leads to conflicting approaches being optimal for different sections of the matrix. The pressure terms are a standard 5-point Poisson stencil (to be extended to 7-point in 3D), and as such would be a good candidate for a hierarchical method using a smoother, such as algebraic multigrid (AMG). However, the forcing terms and coupling sections of the matrix would be unsuitable for this kind of approach. Instead, a standard solver such as CG (Conjugate Gradient) would be better suited.

To tackle this difficulty, we can choose one of two possible approaches: (i) use a suitable pre-conditioner for the system to make it better suited for solution with a standard iterative solver, most likely CG, or (ii) investigate other forms of solvers, such as AMG. While option (ii) could potentially have the greatest

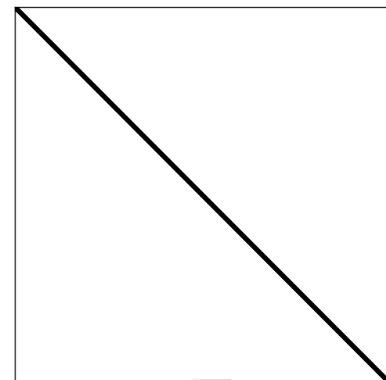


Figure 2: Example of sparsity pattern for  $Q^T B^N Q$  matrix, showing the coupling terms in the right and lower sections of the matrix

effect on both convergence rate and total time to solution, our choices are somewhat limited, given the tools we are using. Either we rely on the smoothed aggregation AMG that is part of *Cusp*, or we would need to develop our own from scratch—at this time there are no other GPU-enabled AMG codes available for public use.

To provide further insight into our options, we can test representative matrices from different applications of our code (with differing complexities of immersed boundaries) and compare a standard CG solver against the form of AMG available in *Cusp*, an aggregative AMG. The CG solver will be used both without a preconditioner, as well as using the diagonal and smoothed-aggregation preconditioners from *Cusp*. For each problem, we show the wall-clock time taken to solve the system to a rela-

tive accuracy of  $10^{-5}$ , the same accuracy used in previous tests. A summary of the matrices produced from each system can be seen in Table 1, and the timing results are shown in Figure 3.

From these results, it can be plainly seen that PCG with smoothed-aggregation AMG as the preconditioner is the fastest on all tests, and so this is the combination of solver and preconditioner used in all our subsequent runs.

Our choice of tools allows us to easily perform all sparse linear algebra operations on the GPU. On the other hand, there are parts of the algorithm that cannot easily be expressed using linear algebra, such as generating the convection term using a finite-difference stencil and applying boundary conditions to the velocities (which involves modifying select values of appropriate arrays). One possible way of performing these actions is to transfer data from the GPU, perform the calculations on the CPU and transfer the modified vector(s) back to the GPU every time step—but this incurs a prohibitively high cost in memory transfers. The alternative, which we have done, is to use custom-written CUDA kernels utilizing all appropriate techniques, including the use of shared memory, to perform these operations on the GPU. This requires access to the underlying data from the *Cusp* data structures, which can be done easily using the *Thrust* library, on which *Cusp* was built.

#### 4. Strategy for GPU implementation

Here we discuss some important implementation details that are used to decrease the total runtime, or to decrease the amount of memory needed, or both.

- *Keep everything on the GPU:* To reduce costly memory transfers, everything that can be performed on the GPU is, regardless of its suitability. For instance, the code to enforce boundary conditions operates on very few values, has almost no computational complexity and is highly divergent based on the boundary conditions chosen (*i.e.*, Dirichlet / Neumann, *etc.*). Thus, it will always perform rather badly on the device, giving essentially no speedup. However, it would take significantly longer to transfer the necessary data back to the host and perform the operation there. This means taking the time to write and test this kernel gives us an overall speedup, due to this elimination of transfers. This is only one example, but all but one element of the total algorithm has been transferred, yielding significant savings in the total run time. The final element still on the CPU involves updating the forcing terms in  $Q$ , and as such involves a very small number of entries compared to any other array. Thus, this transfer ends up being an inconsequential part of the total algorithm.
- *Triple Matrix Product:* To generate the left-hand side of equation (10b), we need to multiply 3 sparse matrices,  $Q^T$ ,  $B^N$  and  $Q$ . To do this within the current *Cusp* framework, we would need to perform two separate matrix-matrix multiplies, the first for  $Q^T B^N$  and then the result of this multiplied by  $Q$ . This method involves creating

a temporary matrix in memory, and for higher-order approximations of  $B^N$ , say,  $3^{rd}$ -order, this temporary can be quite large, in the order of 700MB. *Cusp* performs matrix-matrix multiplies in the following form (using Matlab notation, where  $A[\text{range}, \text{range}]$  denotes a sub matrix of  $A$ , and the ‘:’ symbol denotes all columns/rows depending on context; thus,  $A[\text{slice}, :]$  refers to all columns in a range of rows denoted by  $\text{slice}$ )

**Require:** Input sparse matrices  $A, B$ , result matrix  $C$   
 Split  $A$  into slices  $A[\text{slice}, :]$  s.t. each  $A[\text{slice}, :] \cdot B$  fits in device memory  
**for**  $\forall$  slices **do**  
      $\text{slice} \leftarrow A[\text{slice}, :] \cdot B$   
     add slice to list of slices  
**end for**  
 Assemble  $C$  from all computed slices

The multiplication of  $A[\text{slice}, :] \cdot B$  is here being performed by a helper function within *Cusp* (`cusp::detail::device::spmm_coo_helper`).

We propose a routine to perform a triple matrix product of the form  $D \leftarrow A \cdot B \cdot C$  by using this helper function repeatedly to ensure the full intermediate product need not be calculated. We do this by realizing the following:

```
temp_slice = A[slice,:] * B
D[slice,:] = temp_slice * C.
```

Thus, we can form slices of the final result while only storing a slice as an intermediate by applying the helper function twice in succession. This alleviates the need to create and store the full intermediate matrix. While at first glance the intermediate,  $B^N Q$  might be computed once and used in both (10b) and (10c), we explain below how this term is unnecessary in (10c).

- *Use optimized routines where available:* In equation (10c), we have to calculate the product  $B^N Q \lambda$ , where  $B^N$  and  $Q$  are sparse matrices, and  $\lambda$  is a dense vector. If we implement this naively, we perform the matrix-matrix product of  $B^N Q$  then multiply this with the vector  $\lambda$ . However, the Sparse matrix-vector product (SpMV) in *Cusp* has been optimized to a significant state, as demonstrated by the co-authors of *Cusp*[1]. Therefore, we prefer to implement this operation as a pair of SpMV operations, first  $Q \lambda$  resulting in a vector, then the result of this with  $B^N$ , exchanging the matrix-matrix product with a SpMV. This also reduces the amount of memory needed, as we have no need to store the extra matrix obtained by  $B^N Q$ .
- *Re-use the hierarchy generated by the smoothed-aggregation preconditioner:* The most expensive part of our second solve, Equation (10b) for moving bodies, is the generation of the hierarchy for the smoothed aggregation preconditioner. When bodies are stationary, we have no need to recompute this at each time step, and can use the

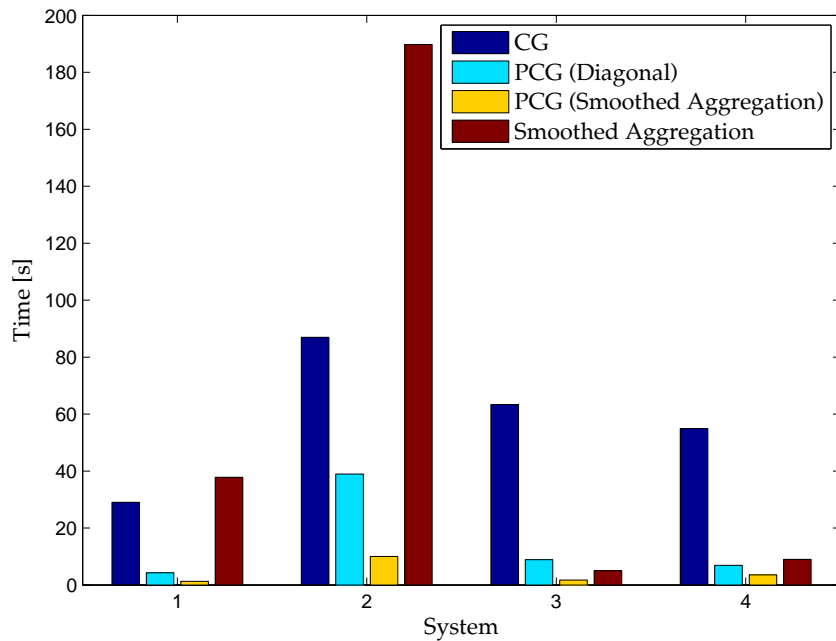


Figure 3: Comparison of GPU solvers on real test problems - Conjugate Gradient, Preconditioned Conjugate Gradient with diagonal and Smoothed Aggregation preconditioners, and a full solve using Smoothed Aggregation

System #	Domain Size	# Bdy Points	# Unknowns	# Non-zeros
1	$330 \times 330$	158	109216	554752
2	$986 \times 986$	786	973768	4914520
3	$930 \times 654$	101	608422	3045406
4	$690 \times 690$	474	477048	2412448

Table 1: Systems 1 and 2 correspond to flow over a cylinder at  $Re = 40$  and  $3000$  respectively, system 3 is for a flapping-wing calculation, and system 4 is from a synthetic test with 3 moving cylinders.

same hierarchy for the entire simulation, effectively amortising the high cost over the total run. When we have moving bodies, this hierarchy should be recalculated every time step. We propose to instead re-use the hierarchy for several time steps. To do so, we need to investigate the balance of not performing the expensive calculation every time step, but potentially having a lower convergence rate for the steps where the hierarchy is re-used. For a flapping airfoil, Figure 4 shows the effect on the total run time of recalculating the preconditioner every  $n$  time steps, clearly showing that in order to reduce run time for this problem, we should recalculate the preconditioner every 2 or 3 time steps.

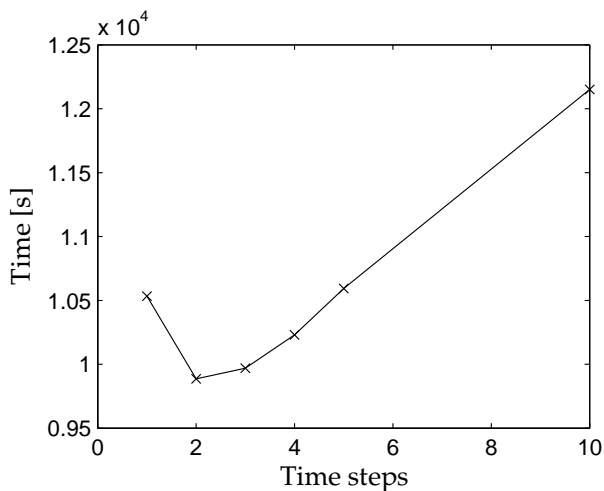


Figure 4: Timings for a flapping airfoil run, re-calculating the Smoothed Aggregation preconditioner every number of time steps.

## 5. Validation

### 5.1. Couette flow between concentric cylinders

As a validation test, we calculate the flow between two concentric cylinders of radius  $r_i = 0.5$  and  $r_o = 1$  centered at the origin. The outer cylinder is held stationary while the inner cylinder is impulsively rotated from rest with an angular velocity of  $\Omega = 0.5$ . The cylinders are contained in a square stationary box of side 1.5 centered at the origin. The fluid in the entire domain is initially at rest and the calculations were carried out for kinematic viscosity  $\nu = 0.03$ .

The steady-state analytical solution for this flow is known. The velocity distribution in the interior of the inner cylinder is the same as for solid body rotation and the azimuthal velocity between the two cylinders is given by:

$$u_\theta(r) = \Omega r_i \frac{(r_o/r - r/r_o)}{(r_o/r_i - r_i/r_o)}. \quad (11)$$

We compared this to the numerical solution for six different grid sizes ranging from  $75 \times 75$  to  $450 \times 450$ . Table 2 shows the  $L^2$  and  $L^\infty$  norms of the relative errors and Figure 5b shows that the scheme is first-order accurate in space, as expected for the IBM formulation we used.

Time	Order of convergence ( $N = 1$ )	Order of convergence ( $N = 3$ )
0.8	0.97	2.67
2	0.99	2.85
4	0.93	2.73
8	0.97	2.83

Table 2: Calculated order of convergence at different times for Couette-flow validation.

To verify the temporal order of convergence, we ran a simulation from  $t = 0$  to  $t = 8$  on a  $151 \times 151$  grid, using different time steps ( $\Delta t = 0.01, 0.005$  and  $0.0025$ ). Both first- and third-order accurate expansions of  $B^N$  were used and the calculated orders of convergence (using the  $L^2$  norms of the differences in the solutions) at various times have been summarised in Table 2, and are as expected.

### 5.2. Flow over an impulsively started cylinder

We also carried out computations to simulate flow over an impulsively started circular cylinder at Reynolds numbers 40, 550 and 3000. The cylinder is of diameter  $d = 1$  centered at the origin and is placed in an external flow with freestream velocity  $u_\infty = 1$ . The domain considered was square with each side of length 30, centered at the origin. The fluid flows from left to right, and the velocity on the left, top and bottom edges was set to be the freestream velocity. A convective boundary condition ( $\frac{\partial u}{\partial t} + u_\infty \frac{\partial u}{\partial x} = 0$ ) was used on the right edge. The initial velocity is uniform throughout the domain. The minimum cell widths used near the solid boundaries were 0.02, 0.01 and 0.004 respectively for the three cases. Away from the body, the grid is an exponential stretched grid. More information about the grids is given in Table 3.

The flow at  $Re40$  reaches a steady state and the drag coefficient was found to be 1.57, which matches the expected value [25]. The vorticity fields and the unsteady drag coefficients for the cases with  $Re550$  and 3000 also agree well with past computations [11]. The results are presented in Figures 6–8.

Re	$n_x \times n_y$	$\Delta x_{min}$	Extent of uniform grid	$r_{stretching}$
40	$330 \times 330$	0.02	$[-0.54, 0.54]$	1.02
550	$450 \times 450$	0.01	$[-0.54, 0.54]$	1.02
3000	$986 \times 986$	0.004	$[-0.52, 0.52]$	1.01

Table 3: Grid information for the impulsively started cylinder cases.

### 5.3. External flow over a circular cylinder

Longer runs were performed to simulate the von Karman street behind a circular cylinder. Table 4 lists the results that were obtained for flows with different Reynolds numbers.

The cylinder is again of diameter 1 and in the center of a domain of size  $30 \times 30$ . The minimum cell width that was used for the runs was 0.02, with it being maintained for the whole distance behind the cylinder. The grid to the left, top and bottom of the cylinder is exponential with a stretching ratio of 1.02.

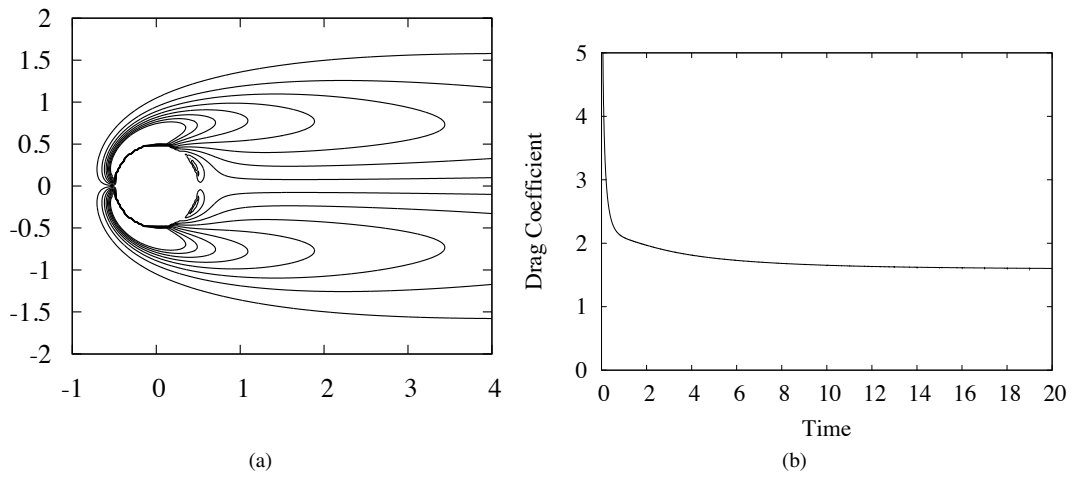


Figure 6: (a) Steady state vorticity field and (b) time varying drag coefficient (b) for external flow over a circular cylinder at Reynolds number 40. The contour lines in (a) are drawn from -3 to 3 in steps of 0.4.

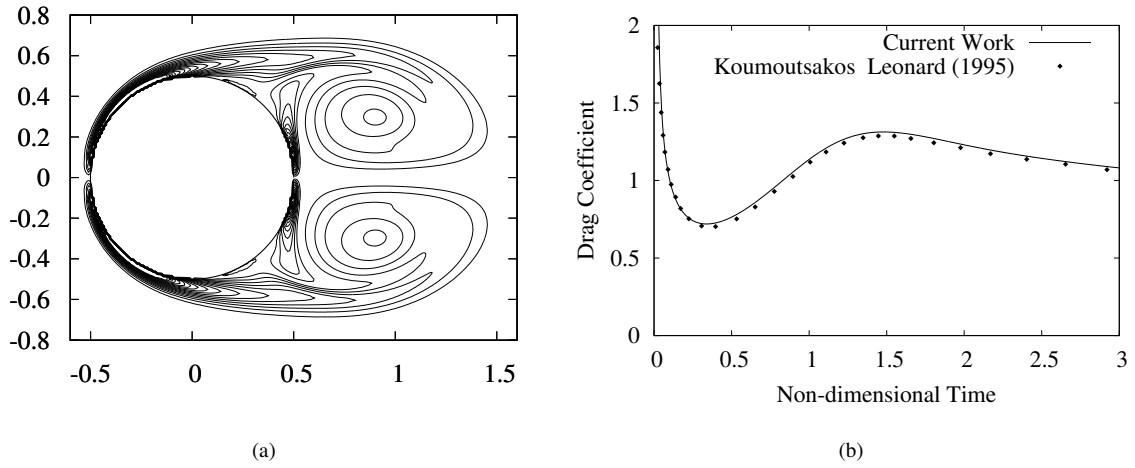


Figure 7: (a) Vorticity field after non-dimensional time 3.0 and (b) time varying drag coefficient for external flow over a circular cylinder at Reynolds number 550. The contour lines in (a) are drawn from -32 to 32 in steps of 2, excluding the zero contour.

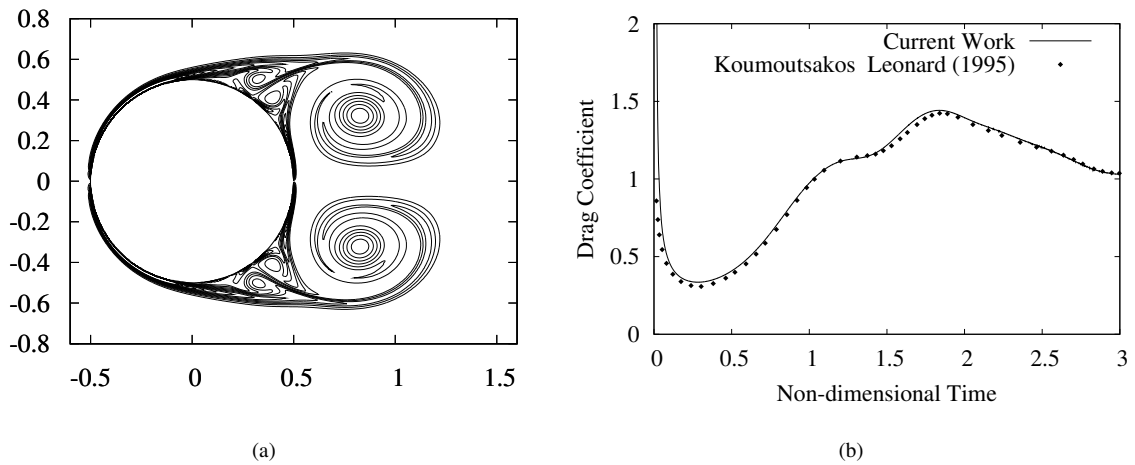
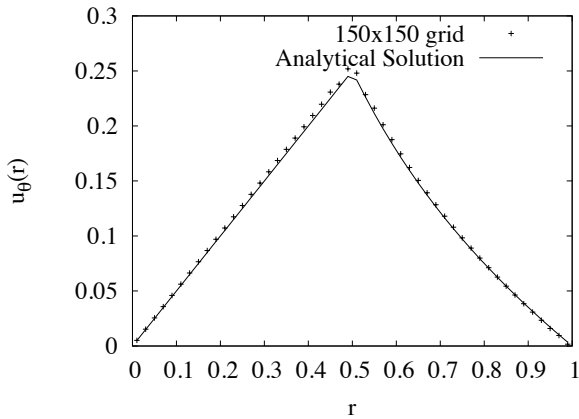
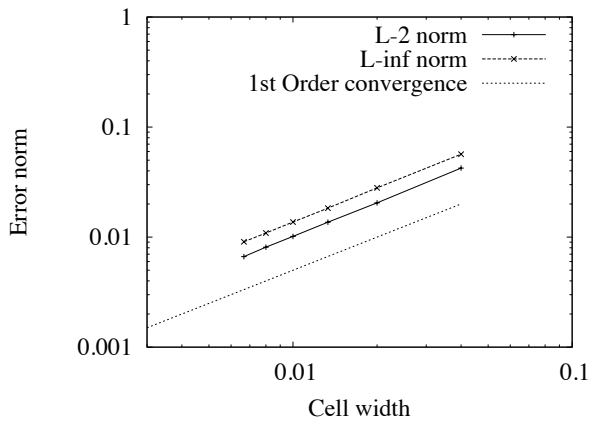


Figure 8: (a) Vorticity field after non-dimensional time 3.0 and (b) time varying drag coefficient for external flow over a circular cylinder at Reynolds number 3000. The contour lines in (a) are drawn from -56 to 56 in steps of 4, excluding the zero contour.





(a)



(b)

Figure 5: (a) Comparison of the numerical solution on a  $150 \times 150$  grid with the analytical solution and (b) convergence study, showing errors for different grid sizes.

The initial position of the cylinder is slightly offset in the  $y$ -direction and it is given a nudge to bring it to the center at the beginning of the run to trigger the instability in the flow and cause vortex shedding.

## 6. Simulations of wake flows and moving boundaries

The calculations presented above validate our code with both analytical results and experimental benchmarks, yet they are not useful to evaluate the performance of the IBM when applied to moving boundary flows. With moving boundaries, the IBM requires regenerating the matrix and the preconditioner at every

$Re$	$C_l$	$C_d$	$St$	$St_{experimental}$ [31]
100	$\pm 0.339$	$1.37 \pm 0.009$	0.166	0.164
150	$\pm 0.532$	$1.35 \pm 0.026$	0.185	0.184
200	$\pm 0.688$	$1.36 \pm 0.042$	0.197	0.197

Table 4: Computed data for flow past a circular cylinder at different Reynolds numbers and comparison with experimental results

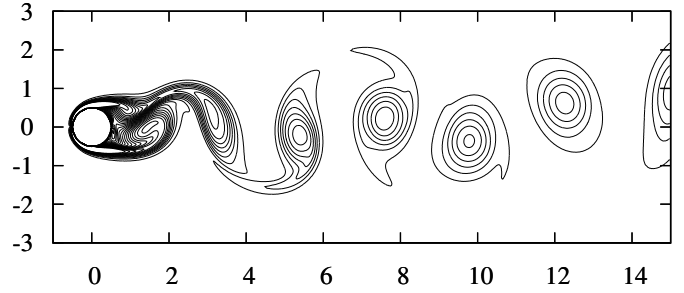


Figure 9: Flow over a circular cylinder at  $Re$  200. Vorticity contours from -5 to 5 in increments of 0.4

time step (or every few time steps). For this reason, we include here some calculations that reproduce past results for flows with moving boundaries, for which we report the run times. All the runs were performed on an NVIDIA Tesla C2050 GPU. The first case is a heaving airfoil placed in a uniform flow (performed by Lewin and Haj-Hariri [13]) and the second is an airfoil that performs both pitching and heaving motions, simulating the flapping motion of an insect wing (performed by Wang et al [30]).

### 6.1. Heaving Airfoil

The simulation was carried out for an elliptic airfoil of thickness-to-chord ratio 0.12 and chord length  $c = 1$ , heaving with a reduced frequency  $k = 2.0$  and non-dimensional maximum heaving velocity  $kh = 0.8$  at Reynolds number  $Re = 500$ . The domain is of size  $30 \times 30$  and the near-body region in  $[-0.52, 0.52] \times [-0.52, 0.52]$  has the minimum cell width of 0.005. The region  $[0.52, 0.78]$  immediately behind the airfoil has an exponential grid with stretching ratio 1.02, and a uniform grid of size 0.01 follows from that region to the edge of the domain. The grid in front of the airfoil is stretched with a ratio of 1.02 and the grid in the  $y$ -direction above and below the body is stretched with a ratio of 1.015. The total size of the mesh is  $1339 \times 686$  and the time step used is 0.0005. The boundary conditions are the same as those used for the earlier cases of external flow over a cylinder. The obtained vorticity field (see Figure 10) compares well with the results of Lewin and Haj-Hariri [13]. The linear solve to calculate the pressure and forces solves for over 900,000 unknowns and each time step of the simulation requires 5 seconds.

### 6.2. Flapping airfoil

We consider a flapping airfoil, the motion of which is described by:

$$x(t) = \frac{A_0}{2} \cos(2\pi ft)$$

$$\alpha(t) = \alpha_0 + \beta \sin(2\pi ft + \phi),$$

where  $x(t)$  is the position of the center of the airfoil and  $\alpha(t)$  is the angle made by the airfoil with the line of oscillation. The airfoil is elliptical with a thickness-to-chord ratio of 0.12 and rotates about its center. The Reynolds number is calculated using the maximum translational velocity of the airfoil and the

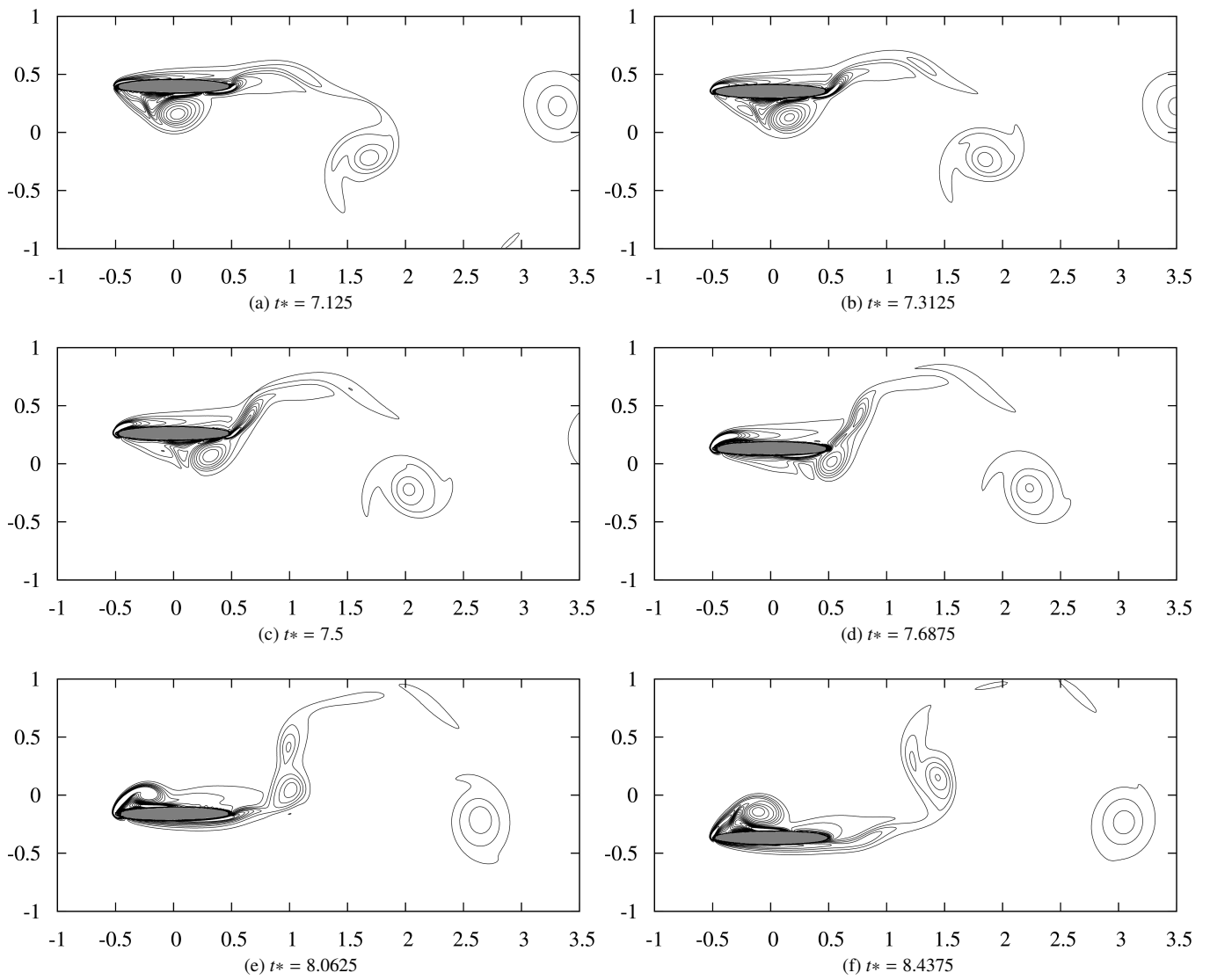


Figure 10: Vorticity field for the downstroke of a heaving airfoil in a flow with  $Re = 500$ ,  $k = 2.0$  and  $kh = 0.8$ . Vorticity contours are drawn at levels  $\pm 2, \pm 6, \pm 10, \text{etc.}$  Compare with Figure 3 in [13].

chord length. We consider the case with symmetrical rotation ( $\phi = 0$ ) at Reynolds number 75 and with  $A_0/c = 2.8$ ,  $\alpha = \pi/2$ ,  $\beta = \pi/4$  and  $f = 0.25$  Hz.

The airfoil has chord length 1 and oscillates at the center of a domain, each side of which is 30 chord-lengths long. The grid is uniform in the region  $[-2, 2] \times [-0.52, 0.52]$  with cell width 0.01 and beyond this region it is stretched with a ratio of 1.01 on all sides, resulting in a mesh size of  $930 \times 654$  cells. The time step used is 0.001. The run time for 4000 time steps (one cycle) was 164 seconds, when the preconditioner was updated every two time steps.

The vorticity field at different times during the first cycle is shown in Figure 11 and a comparison of the unsteady lift coefficient with the computational and experimental results presented by Wang et al [30] is plotted in Figure 12. The experiments were conducted with a three-dimensional wing and both simulations were performed in two dimensions, hence we don't expect them to closely match. But we note that the computational results follow the expected trend and agree reasonably well with the experimental results.

## 7. Conclusions and Future Work

At this time, we have a validated GPU code for the projection IBM, and we have shown convergence with the expected rates. Using the free and open-source *Cusp* and *Thrust* libraries to provide sparse linear algebra functionality, we are able to quickly run large experiments to test a wide variety of problems including internal Couette flows, external flows past cylinders and complex moving bodies.

In this paper we have outlined a strategy for using the *Cusp* library effectively by reducing memory transfers between the host and device and where possible prioritizing the use of the most tuned routines. We save the limited memory available on the GPU by using a modified routine to calculate a necessary triple matrix product without needing a costly intermediate matrix. Furthermore, we have investigated the suitability of a variety of linear solvers for our particular problem, demonstrating that for our problems a Conjugate Gradient method with a smoothed aggregation AMG preconditioner updated every 2 or 3 timesteps is the best available for reducing the total runtime of the algorithm.

We have demonstrated the capability of our code for both high Reynolds number flows and for flows with complex moving boundaries, comparing very well with existing works.

The next major step for this work, is to extend our algorithm into 3 dimensions—while this extension doesn't involve many differences to the equations, it will require a significant increase in memory usage. This will necessitate modifying the code to run in parallel on multiple GPUs, a far more significant change. A further improvement would be to implement the IBM with an adaptive grid – this would reduce both the memory requirements and the amount of work needed per timestep.

## 8. Acknowledgments

We acknowledge support from NSF grant OCI-0946441, ONR award #N00014-11-1-0356, and Boston University College of Engineering. LAB is also grateful of the support from NVIDIA via an Academic Partnership award.

## References

## References

- [1] Nathan Bell and Michael Garland. Implementing sparse matrix-vector multiplication on throughput-oriented processors. In *SC'09: Proceedings of the Conference on High Performance Computing Networking, Storage and Analysis*, pages 1–11, New York, NY, USA, 2009. ACM.
- [2] A. J. Chorin. Numerical solution of the Navier-Stokes equations. *Math. Comp.*, 22(104):745, October 1968.
- [3] T. Colonius and K. Taira. A fast immersed boundary method using a nullspace approach and multi-domain far-field boundary conditions. *Computer Methods in Applied Mechanics and Engineering*, 197(25-28):2131–2146, 2008.
- [4] E Fadlun. Combined Immersed-Boundary Finite-Difference Methods for Three-Dimensional Complex Flow Simulations. *J. Comp. Phys.*, 161(1):35–60, June 2000.
- [5] Reza Ghias, Rajat Mittal, and T.S. Lund. A non-body conformal grid method for simulation of compressible flows with complex immersed boundaries. *AIAA Paper*, 80(January):2004, 2004.
- [6] D Goldstein, R Handler, and L Sirovich. Modeling a No-Slip Flow Boundary with an External Force Field. *J. Comp. Phys.*, 1993.
- [7] Gianluca Iaccarino and Roberto Verzicco. Immersed boundary technique for turbulent flow simulations. *Applied Mechanics Reviews*, 56(3):331, 2003.
- [8] G. Kalitzin and Gianluca Iaccarino. Toward immersed boundary simulation of high Reynolds number flows. *Annual Research Briefs*, 2003.
- [9] J. Kim and P. Moin. Application of a fractional-step method to incompressible Navier-Stokes equations. *J. Comp. Phys.*, 59(2):308–323, 1985.
- [10] Jungwoo Kim, Dongjoo Kim, and Haecheon Choi. An Immersed-Boundary Finite-Volume Method for Simulations of Flow in Complex Geometries. *J. Comp. Phys.*, 171(1):132–150, July 2001.
- [11] P Koumoutsakos and A Leonard. High-resolution simulations of the flow around an impulsively started cylinder using vortex methods. *Journal of Fluid Mechanics*, 296:1–38, 1995.
- [12] M.C. Lai and Charles S Peskin. An immersed boundary method with formal second-order accuracy and reduced numerical viscosity. *J. Comp. Phys.*, 160(2):705–719, 2000.
- [13] G C Lewin and H Haj-Hariri. Modelling thrust generation of a two-dimensional heaving airfoil in a viscous flow. *J. Fluid Mech.*, 492:339–362, 2003.
- [14] S. Majumdar, Gianluca Iaccarino, and Paul Durbin. RANS solvers with adaptive structured boundary non-conforming grids. *Annual Research Briefs*, pages 353–366, 2001.
- [15] S Marella, S Krishnan, H Liu, and H Udaykumar. Sharp interface Cartesian grid method I: An easily implemented technique for 3D moving boundary computations. *J. Comp. Phys.*, 210(1):1–31, November 2005.
- [16] R Mittal, C Bonilla, and H S Udaykumar. Cartesian grid methods for simulating flows with moving boundaries. In *Computational Methods and Experimental Measurements XI*, pages 557–566, 2003.
- [17] R. Mittal and G. Iaccarino. Immersed boundary methods. *Ann. Rev. Fluid Mech.*, 37(1):239–261, 2005.
- [18] R Mittal, Y Utturkar, and HS Udaykumar. Computational modeling and analysis of biomimetic flight mechanisms. *AIAA Paper*, 865:2002, 2002.
- [19] J. Mohd-Yusof. Development of immersed boundary methods for complex geometries. *Annual Research Briefs*, pages 325–336, 1998.
- [20] J. B. Perot. An analysis of the fractional step method. *J. Comp. Phys.*, 108(1):51–58, 1993.
- [21] C.S. Peskin. Flow patterns around heart valves: A numerical method. *J. Comp. Phys.*, 10(2):252–271, 1972.
- [22] a Roma. An Adaptive Version of the Immersed Boundary Method. *J. Comp. Phys.*, 153(2):509–534, August 1999.

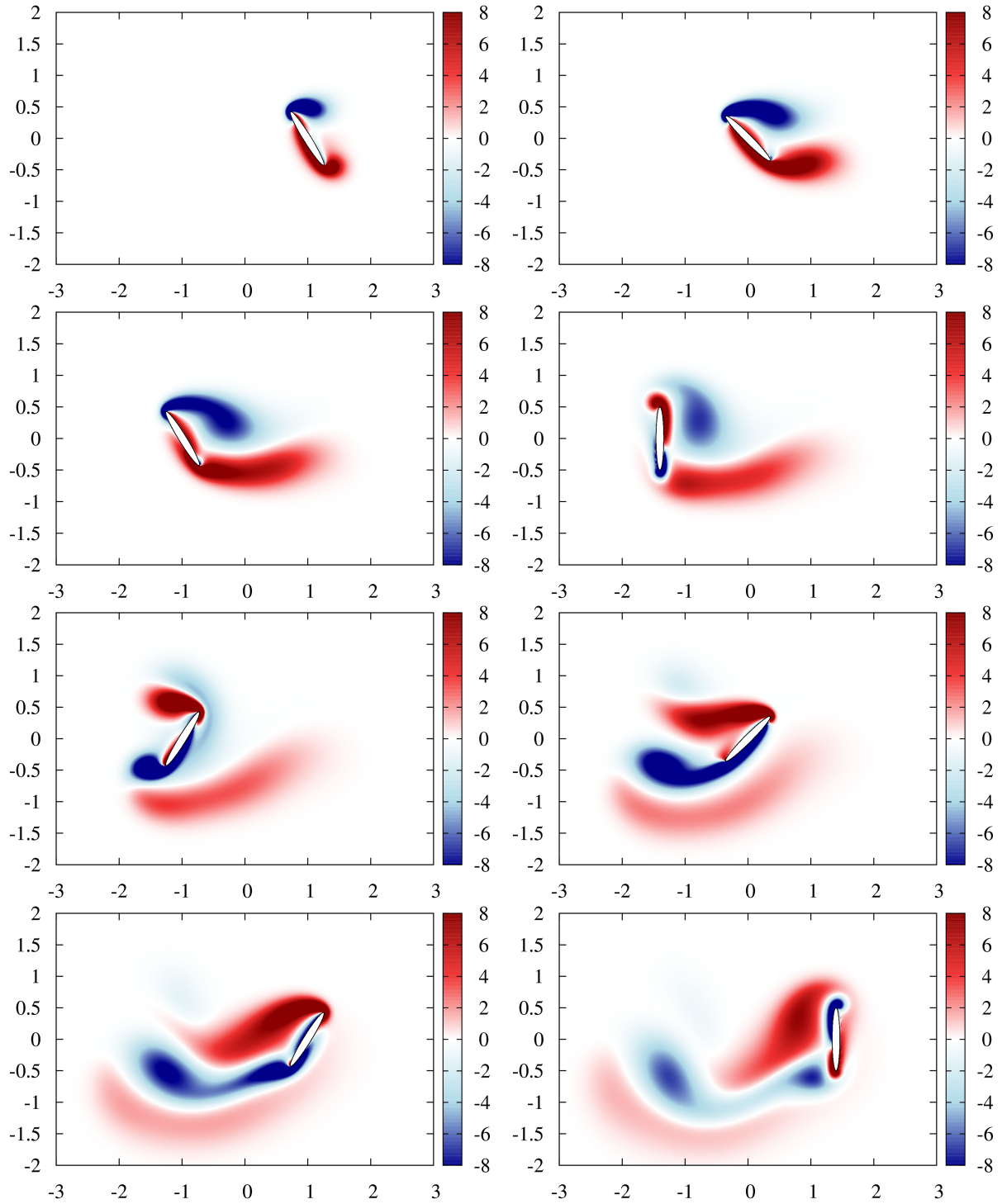


Figure 11: Vorticity field around a flapping airfoil with symmetric rotation ( $\phi = 0$ ,  $A_0/c = 2.8$ ) at Reynolds number 75. The frames represent equally spaced instances of time in the first cycle of flapping:  $T = 0.125, 0.25, 0.375, \dots$  (The time is non-dimensionalised by the time period of oscillation)

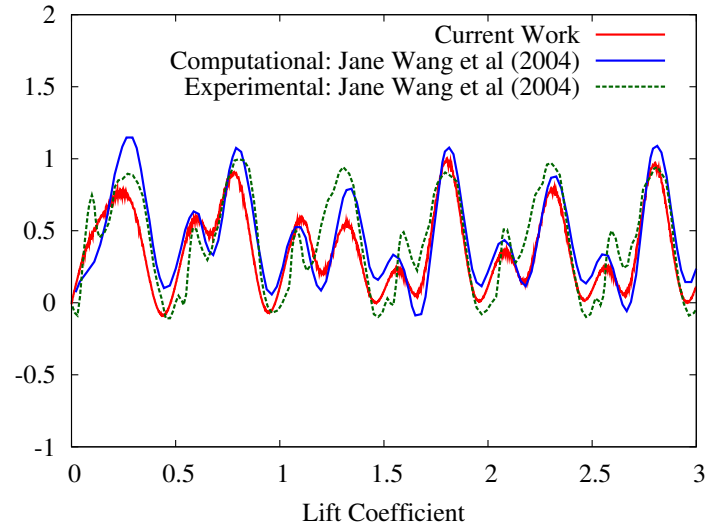


Figure 12: Unsteady lift coefficient for the first three cycles of a flapping airfoil ( $Re = 75$ ,  $\phi = 0$ ,  $A_0/c = 2.8$ ). The time is non-dimensionalised using the time period of oscillation and the lift coefficient is calculated by normalising the lift force with respect to the maximum of the quasi-steady force experienced by the airfoil considered (see [30] for more details)

- [23] E M Saiki and S Biringen. Numerical Simulation of a Cylinder in Uniform Flow: Application of a Virtual Boundary Method. *J. Comp. Phys.*, 123(2):450–465, February 1996.
- [24] K. Taira and T. Colonius. The immersed boundary method: A projection approach. *J. Comp. Phys.*, 225(2):2118–2137, 2007.
- [25] D. J. Tritton. Experiments on the flow past a circular cylinder at low Reynolds numbers. *J. Fluid Mech.*, 6(04):547–567, 1959.
- [26] H Udaykumar. Multiphase Dynamics in Arbitrary Geometries on Fixed Cartesian Grids. *J. Comp. Phys.*, 137(2):366–405, November 1997.
- [27] H Udaykumar. Computation of Solid–Liquid Phase Fronts in the Sharp Interface Limit on Fixed Grids. *J. Comp. Phys.*, 153(2):535–574, August 1999.
- [28] H Udaykumar. A Sharp Interface Cartesian Grid Method for Simulating Flows with Complex Moving Boundaries. *J. Comp. Phys.*, 174(1):345–380, November 2001.
- [29] M Uhlmann. An immersed boundary method with direct forcing for the simulation of particulate flows. *J. Comp. Phys.*, 209(2):448–476, November 2005.
- [30] Z Jane Wang, James M Birch, and Michael H Dickinson. Unsteady forces and flows in low reynolds number hovering flight: two-dimensional computations vs robotic wing experiments. *The Journal of Experimental Biology*, 207:449–460, 2004.
- [31] C H K Williamson. Vortex dynamics in the cylinder wake. *Ann. Rev. Fluid Mech.*, 28:477–539, 1996.
- [32] T Ye. An Accurate Cartesian Grid Method for Viscous Incompressible Flows with Complex Immersed Boundaries. *J. Comp. Phys.*, 156(2):209–240, December 1999.